PERFORMANCE ANALYSIS OF HYBRID ENERGY STORAGE SYSTEM-BASED DC MICROGRID FOR A DEVELOPED CONTROL TECHNIQUE

Mahesh Kumar* and Mylavarapu Ramamoorty**

Abstract

This work proposes a control technique for the operation of the proposed DC microgrid (DCMG) consisting of a Hybrid Energy Storage System (HESS). The dynamic performance analysis of DCMG for the developed control scheme has been carried out in islanded mode under several operating conditions. In DCMG, the HESS consists of Battery Energy Storage System (BESS) and Hydrogen Storage System (H_2SS). The bidirectional dc-dc converter and dc-dc buck converter have been used to integrate BESS and H_2SS, respectively, into DCMG. In the islanded mode, during power mismatch in DCMG, the proposed control scheme allows to control the operation of BESS to fulfil the power mismatch, and beyond the capacity of BESS, the surplus generated power is stored in the H_2SS. The proposed control scheme is aimed to manage the power and rated voltage of DCMG for all cases.

Key Words

DC microgrid, hybrid energy storage system, hydrogen storage system, DC–DC converters, power management

1. Introduction

For underdeveloped and developing countries, the remote rural areas may not have access to the electric power supply from the main grid. The Renewable Energy Sources (RESs) such as Wind Turbine (WT), solar Photovoltaic (PV), and fuel cell Distributed Generations (DGs) have an important role in the remote rural areas, which are developing fast and have attracted increased interests of the researchers and utilities due to various environmental, economical, and technical advantages offered by them [1]. Due to the intermittent nature of renewable sources, the direct connection of the renewable sources to the main grid would create several issues such as voltage fluctuations, frequency variation, and protection and stability issues [2], [3]. However, the utility grid may not be available in the remote rural areas. Therefore, the microgrid (AC or DC) provides the facility for the connections of various DGs and Energy Storage Systems (ESSs). The DC Microgrid (DCMG) has many advantages over the AC microgrid as follows: (1) better reliability; (2) ease control of each DG by controlling only DCMG voltage; (3) higher efficiency due to lower losses; (4) no synchronization required for interconnecting many DGs; and (5) better controllability due to the absence of reactive power, phase, and frequency control [4], [5]. The Hybrid Energy Storage System (HESS) based DCMG is designed for feeding the power supply to the remote rural areas, independently.

The Pulse-Width Modulation (PWM)-based Voltage Source Converters (VSCs) provide rated voltage, high-quality power conversion, power flow control, fault protection, system balancing, and maximum power point tracking of various DGs [1]–[4]. In [6], a control strategy of three-phase back-to-back PWM VSC is presented for a doubly fed induction generator for controlling the power generation in the WT DG. The same control strategy has been implemented in the proposed DCMG in this work. The demonstrated DCMG consists of various renewable DGs such as Solid-Oxide Fuel Cell (SOFC), WT, PV, and ESSs along with the loads. In [7], a control strategy of single-phase voltage controlled Voltage Source Inverter (VSI) based on two revolving field theory principle is presented for integrating single-phase AC static as well as dynamic loads into the DCMG. The same control strategy is implemented for integrating the single-phase AC loads into the proposed DCMG in this work.

For maintaining the stability of DCMG, the power should be balanced at all times in the DCMG. Due to intermittent nature of the renewable sources because of variable generations and loads of the DCMG in islanded mode, the controllable DGs, *i.e.,* SOFC and ESSs, are

* Electrical and Electronics Engineering Department, Amity School of Engineering and Technology, Amity University Haryana, Gurugram, India; e-mail: singhrmkumar@gmail.com

** Electrical Engineering Department, Vallurupalli Nageswara Rao Vignana Jyothi Institute of Engineering and Technology, Hyderabad, India; e-mail: mrmoorty@gmail.com

Corresponding author: Mahesh Kumar

Recommended by Prof. Ikhlaq Hussain
(DOI: 10.2316/J.2022.203-0379)

necessary for balancing the power in the DCMG. Various ESSs such as battery, supercapacitor, and flywheel are being used. Generally, Battery Energy Storage System (BESS) is preferred amongst several ESSs due to its fast response and long-term output power [8]. However, the BESS has limited storage capacity. Beyond the rated capacity of the BESS, under islanded mode, there may be deficit or surplus power in the DCMG, and then another ESS is needed.

To resolve this problem, an additional ESS such as hydrogen storage can be used along with the BESS in an islanded mode microgrid. The Hydrogen Storage System (H_2SS) is a good option for energy storage for long term. Therefore, an HESS consisting of the BESS and H_2SS, has been suggested for overcoming the problem of the power balance at the proposed DCMG under islanded mode. The BESS and H_2SS are interconnected to the DCMG through the Bidirectional DC–DC Converter (BDC) and DC–DC buck converter, respectively.

In this paper, a control technique of the HESS, integrated into the DCMG, is proposed for maintaining the power mismatch at the islanded DCMG under various operating conditions. A power control algorithm has also been developed for the operation of the DCMG along with the HESS in islanded mode. The developed control scheme allows to control the operation of the BESS up to its rated capacity, and thereafter store the generated surplus power in the H_2SS. The main contribution and the novelty in this paper are expressed as follows:

- A HESS has been considered for managing the power mismatch in a single DCMG.
- Developed a control strategy of HESS integrated into the DCMG for controlling the operation of the BESS as well as the H_2SS for power management in the DCMG under islanded mode for all cases.
- The proposed control strategy uses three voltage controllers and one current controller, in which a current controller and two voltage controllers are used for the converter of the BESS, and a third voltage controller is used for the converter of H_2SS.
- IEEE-1547 standard is in compliance with the developed control technique.

2. Modelling and Configuration of DCMG

2.1 Configuration of DC Microgrid

The architecture of a HESS-based DCMG with various renewable DGs is shown in Fig. 1. In the proposed DCMG, the decentralized control technique is used, which eliminates the circulating current between the various DGs of the DCMG. The decentralized control scheme can be achieved by using the constant rated DCMG voltage as common reference signals for controlling all DGs, without any communication link. From the study of several literature [3], [4], [7], [9]–[11], a 750 V DC voltage of the DCMG is considered in the present study, which eliminates the transformer on the load side VSCs.

In the developed DCMG, a 200 kW, Wind Turbine Generator (WTG) using a doubly fed induction machine is connected to the DCMG using the three-phase VSC. A 100 kW PV system and a 50 kW SOFC DG have been interconnected to the DCMG using the DC–DC boost converters for boosting the low generated DC voltage. The HESS consisting of the BESS and H_2SS is integrated into the DCMG through the BDC and DC–DC buck converter, respectively. Beyond the charging capacity of the BESS, the continuously generated surplus power is being used to store in hydrogen form in the H_2SS for a long time. The electrical energy is converted into hydrogen by using the

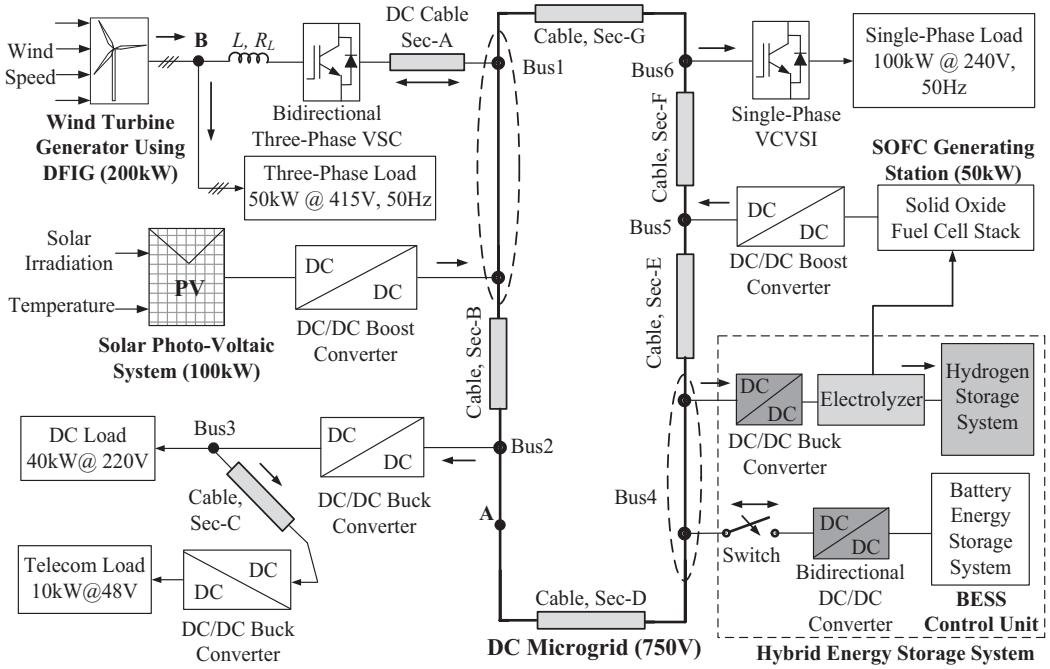

Figure 1. Architecture of hybrid energy storage system-based DC microgrid.

electrolysis process through the electrolyzer [9], [12], [13]. If the WT and PV DGs along with the BESS, are unable to fulfil the load demand, then the stored hydrogen will be used to regenerate the electricity using the SOFC DG and electrolyzer. The H_2SS along with the battery has been considered in the HESS, because the surplus power storage capacity in the H_2SS with the consideration of large storage tank does not have any limitations.

The electrochemical reactions in the electrolyzer, using the electricity, are expressed in [12], [13].

$$\left.\begin{aligned}&\text{Anode}: 2\text{OH}^- \rightarrow \tfrac{1}{2}\text{O}_2 \uparrow + \text{H}_2\text{O} + 2\text{e}^-\\&\text{Cathode}: \text{H}_2\text{O} + 2\text{e}^- \rightarrow \text{H}_2 \uparrow + 2\text{OH}^-\end{aligned}\right\}.$$

The valve regulated lead acid battery of 100 kW, 375 V, 550 Ah for 2 h is considered for the BESS. Under maximum power generation and minimum load demand case in the DCMG, considering BESS fully charged, the continuously generated maximum surplus power may be 216 kW. Thus, the power rating of the DC–DC buck converter, used for integrating H_2SS including electrolyzer and storage tank into the DCMG, is considered as 270 kW. The parameters used for an electrolyzer (40 kW rating) of the H_2SS are taken from [12]. For the available current rating (735 A) of the DC cable, based on maximum current in the DCMG, the parameters of DC cables like DC resistance (0.047 Ω/km) and overall diameter (33.9 mm) are taken from [14]. The parameters used for the proposed DCMG are given in Table 3, in Appendix.

In this paper, the control strategies for three-phase VSC of WTG, and for DC–DC boost converters of SOFC and PV systems, are considered the same as proposed in [4]. The DCMG voltage has been maintained constant through the control strategy of three-phase VSC of WTG for all operating conditions. The loads integrated into the DCMG are: (1) 100 kW single-phase AC load; (2) 40 kW DC load operating at 220 V; (3) 10 kW telecommunication load operating at 48 V DC voltage; and (4) 50 kW three-phase load connected in the local area of WTG. Thus, the total rated load is 200 kW.

2.2 Modelling of DC Microgrid

2.2.1 Modelling of the Distributed Generations

The dynamic modelling equations for SOFC, PV, and WT DGs, BESS, and various converters are taken from [4], [12], [15]–[18].

2.2.2 Modelling of Hydrogen Energy Storage System

The modelling of an alkaline-type electrolyzer has been described below. The reversible voltage (V_{rev}) or thermodynamic cell voltage (V_0) solely depends on Gibb's energy (ΔG) and is given in (1) [12], [13].

$$\left.V_{rev} = \frac{\Delta G}{\text{F}N_e} = V_0 \quad \text{and} \quad V_{Elz,0} = V_0 \times N_{cell,Elz}\right\}, \quad (1)$$

where F is the constant of Faraday, $V_{Elz,0}$ is the no-load voltage of electrolyzer, N_e is the number of electrons in one reaction, and $N_{cell,Elz}$ is the number of cells connected in series in one stack.

The Faraday efficiency (η_I) of the electrolyzer is expressed by (2). The volumetric flow rate of hydrogen ($\dot{U}_H$), hydrogen molar production rate ($M_{H,Prod}$) as a function of current, and V–I relationship of the electrolyzer are expressed by (3), (4), and (5), respectively [12], [13].

$$\left.\begin{aligned}&\eta_I = \tfrac{J_{Elz}^2}{K_1+J_{Elz}^2}K_2;\ \text{where},\ J_{Elz} = \tfrac{I_{Elz}}{A_{Elz}},\quad I_{Elz} = \tfrac{P_{Elz}}{V_{Elz,0}}\\&\text{and},\quad K_1 = 50 + 2.5T_{Elz},\quad K_2 = 1 - 0.00075T_{Elz}\end{aligned}\right\}, \quad (2)$$

$$\dot{U}_H = M_{H,prod} \times v_t \times 3600\ (\text{Ltr/hr}), \quad (3)$$

$$\left.\begin{aligned}&M_{H,prod} = \eta_I I_{Elz}\tfrac{N_{Elz}}{FN_e},\quad \text{and}\\&I_{Elz} = N_{Stack,Elz} * I_{Elz,Stack}\end{aligned}\right\}, \quad (4)$$

$$\left.\begin{aligned}&V_{cell,Elz} = V_0 + I_{Elz,stack}\left(\tfrac{r_1+r_2T_{Elz}}{A_{Elz}}\right)\\&+V_1\log\left(\tfrac{m_1+(m_2/T_{Elz})+(m_3/T_{Elz}^2)}{A_{Elz}}I_{Elz,stack}+1\right)\\&\text{and},\quad V_{Elz} = V_{cell,Elz} * N_{cell,Elz,stack}\end{aligned}\right\}, \quad (5)$$

where J_{Elz} is the current density of electrolyzer, I_{Elz} is the total rated current of electrolyzer, A_{Elz} is the area of a stack of electrolyzer, P_{Elz} is the rated power of electrolyzer, K_1 and K_2 are the parameters related to Faraday efficiency, v_t is the molar volume of ideal gas, $V_{cell,Elz}$ is the voltage across one cell of electrolyzer, $I_{Elz,stack}$ is the current in one stack of electrolyzer, $N_{stack,Elz}$ is number of parallel stacks of electrolyzer, T_{Elz} is electrolyzer temperature, V_{Elz} is the rated load voltage of electrolyzer, r_1 and r_2 are the parameters of Ohmic resistances, V_1 is overvoltage of electrolyzer, and m_1, m_2, m_3 are overvoltage coefficients of electrolyzer.

2.2.3 Modelling of DC–DC Converters

The BDC and DC–DC buck converter are shown in Fig. 2(a) and (b), respectively [1], [4]. The average voltage of inductor and average capacitor current equations of DC–DC buck converter, as shown in Fig. 2(b), are expressed by (6) and (7), and are as follows:

$$\left.\begin{aligned}&\frac{d}{dt}\langle i_L\rangle = \frac{\langle v_{in}d\rangle}{L_{\text{buck}}} - \frac{\langle v_{o\_\text{buck}}\rangle}{L_{\text{buck}}}\quad \text{and}\\&\frac{d}{dt}\langle v_{o\_\text{buck}}\rangle = \frac{\langle i_L\rangle}{C_{o\_\text{buck}}} - \frac{\langle v_{o\_\text{buck}}\rangle}{R_{L,dc}C_{o\_\text{buck}}}\end{aligned}\right\}, \quad (6)$$

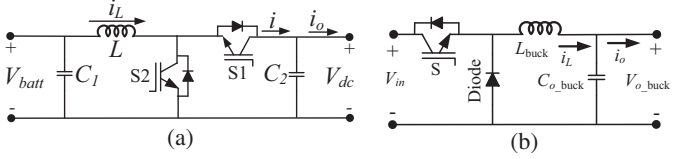

Figure 2. (a) DC–DC bidirectional converter and (b) DC–DC buck converter.

$$\left.\begin{aligned} \frac{d}{dt}I_L &= \frac{DV_{in}}{L_{\text{buck}}} - \frac{V_{o\_\text{buck}}}{L_{\text{buck}}} \quad \text{and} \\ \frac{d}{dt}V_{o\_\text{buck}} &= \frac{I_L}{C_{o\_\text{buck}}} - \frac{V_{o\_\text{buck}}}{R_{L,dc}C_{o\_\text{buck}}} \end{aligned}\right\}, \tag{7}$$

where V_{o_buck} and V_{dc} are output and input DC voltage, respectively, D is the average value of duty cycle, C_{o_buck} and L_{buck} are output capacitor and inductor of buck converter, respectively, I_o is the average value of output current, I_L is current through the inductor, and $R_{L,DC}$ is the resistive DC load across the output terminals.

By considering small perturbations for all quantities as, $v_{in} = V_{in} + \tilde{v}_{in}$, $v_{0\_buck} = V_{o\_buck} + \tilde{v}_{o\_buck}$, $d = D + \tilde{d}$, $i_L + \tilde{i}_L$, and $i_o = I_o + \tilde{i}_o$, and by solving (6) and (7), the small-signal state-space model of DC–DC converter in buck mode is represented by (8).

$$\left.\begin{aligned} \frac{d}{dt}\begin{bmatrix} \tilde{i}_L \\ \tilde{v}_{o\_\text{buck}} \end{bmatrix} &= \begin{bmatrix} 0 & -1/L_{\text{buck}} \\ \frac{1}{C_{o\_\text{buck}}} & \frac{-1}{R_{L,dc}C_{o\_\text{buck}}} \end{bmatrix}\begin{bmatrix} \tilde{i}_L \\ \tilde{v}_{o\_\text{buck}} \end{bmatrix} + \begin{bmatrix} \frac{D}{L_{\text{buck}}} \\ 0 \end{bmatrix}\tilde{v}_{in} + \begin{bmatrix} \frac{V_{in}}{L_{\text{buck}}} \\ 0 \end{bmatrix}\tilde{d} \\ \text{output}(Y_{\text{buck}}) = [\tilde{v}_{o\_\text{buck}}] &= \begin{bmatrix} 0 & 1 \end{bmatrix}\begin{bmatrix} \tilde{i}_L \\ \tilde{v}_{o\_\text{buck}} \end{bmatrix}, \text{ where, } V_{o\_\text{buck}} = V_{Elz} \text{ and } V_{in} = V_{dc} \end{aligned}\right\}. \tag{8}$$

The quantities represented as v_{in}, v_{o_buck}, i_L, i_o, and d are instantaneous values. The quantities represented as V_{in}, V_{o_buck}, I_L, I_o, and D are average values. The quantities represented with tilde, $\tilde{v}_{in}$, $\tilde{v}_{o\_\text{buck}}$, $\tilde{v}_{dc}$, $\tilde{v}_{Elz}$, $\tilde{i}_L$, $\tilde{i}_o$, and $\tilde{d}$ are perturbations in the various quantities. The controlled transfer function, $G_{C\_buck(s)}$, of DC–DC buck converter is expressed using (8), and is given by (9).

$$G_{C\_\text{buck}}(s) = \left.\frac{\tilde{v}_{Elz}(s)}{\tilde{d}(s)}\right|_{\tilde{v}_{dc}=0} = \frac{V_{dc}}{L_{\text{buck}}C_{o\_\text{buck}}s^2 + (L_{\text{buck}}/R_{L,dc})\,s + 1}. \tag{9}$$

The equations (10) and (11) represent the small-signal state-space model of the BDC, as shown in Fig. 2(a), for the buck as well as the boost mode, respectively.

$$\left.\begin{aligned} \tfrac{d}{dt}\begin{bmatrix} \tilde{i}_L \\ \tilde{v}_{Batt} \end{bmatrix} &= \begin{bmatrix} -R_1/L & -1/L \\ 1/C_1 & 0 \end{bmatrix}\begin{bmatrix} \tilde{i}_L \\ \tilde{v}_{Batt} \end{bmatrix} + \begin{bmatrix} V_{dc}/L \\ 0 \end{bmatrix}\tilde{d} + \begin{bmatrix} D/L \\ 0 \end{bmatrix}\tilde{v}_{dc} + \begin{bmatrix} 0 \\ -1/C_1 \end{bmatrix}\tilde{i}_o \\ \text{output}(\mathbf{Y}_{\text{BDC\_buck}}) &= \begin{bmatrix} \tilde{i}_L \\ \tilde{v}_{Batt} \\ \tilde{i}_o \end{bmatrix} = \begin{bmatrix} 1 & 0 \\ 0 & 1 \\ 1 & 0 \end{bmatrix}\begin{bmatrix} \tilde{i}_L \\ \tilde{v}_{Batt} \end{bmatrix}, \quad \text{where, } V_o = V_{Batt} \quad \text{and} \quad V_{in} = V_{dc} \end{aligned}\right\}, \tag{10}$$

$$\left.\begin{aligned} \tfrac{d}{dt}\begin{bmatrix} \tilde{i}_L \\ \tilde{v}_{dc} \end{bmatrix} &= \begin{bmatrix} -R_1/L & -(1-D)/L \\ (1-D)/C_2 & 0 \end{bmatrix}\begin{bmatrix} \tilde{i}_L \\ \tilde{v}_{dc} \end{bmatrix} + \begin{bmatrix} -V_{dc}/L \\ -I_L/C_2 \end{bmatrix}\tilde{d} + \begin{bmatrix} 1/L \\ 0 \end{bmatrix}\tilde{v}_{Batt} + \begin{bmatrix} 0 \\ -1/C_2 \end{bmatrix}\tilde{i}_o \\ \text{output}(\mathbf{Y}_{\text{BDC\_boost}}) &= \begin{bmatrix} \tilde{i}_L \\ \tilde{v}_{dc} \\ \tilde{i}_o \end{bmatrix} = \begin{bmatrix} 1 & 0 \\ 0 & 1 \\ (1-D) & 0 \end{bmatrix}\begin{bmatrix} \tilde{i}_L \\ \tilde{v}_{dc} \end{bmatrix} + \begin{bmatrix} 0 \\ 0 \\ -I_L \end{bmatrix}\tilde{d}, \quad \text{where, } V_{in} = V_{Batt} \text{ and } V_o = V_{dc} \end{aligned}\right\}. \tag{11}$$

The controllable transfer functions of the BDC in buck mode have been expressed using (10) and are given by (12). The controllable transfer functions of the BDC in boost mode have been derived from (11) and are expressed by (13).

$$\left.\begin{aligned} G_{C,1\_\text{buck}}(s) &= \left.\frac{\tilde{i}_L(s)}{\tilde{d}(s)}\right|_{\tilde{v}_{dc}=\tilde{i}_o=0} = \frac{V_{dc}C_1 s}{LC_1s^2 + R_1C_1s + 1} = \left.\frac{\tilde{i}_o(s)}{\tilde{d}(s)}\right|_{\tilde{v}_{dc}=\tilde{i}_o=0} = G_{C,3\_\text{buck}}(s) \\ G_{C,2\_\text{buck}}(s) &= \left.\frac{\tilde{v}_{Batt}(s)}{\tilde{d}(s)}\right|_{\tilde{v}_{dc}=\tilde{i}_o=0} = \frac{V_{dc}}{LC_1s^2 + R_1C_1s + 1} \end{aligned}\right\}, \tag{12}$$

$$\left.\begin{aligned} G_{C,1\_boost}(s) &= \left.\frac{\tilde{i}_L(s)}{\tilde{d}(s)}\right|_{\tilde{v}_{Batt}=\tilde{i}_o=0} = \frac{V_{dc}C_2 s + (1-D)I_L}{LC_2 s^2 + R_1 C_2 s + (1-D)^2} \\ G_{C,2\_boost}(s) &= \left.\frac{\tilde{v}_{dc}(s)}{\tilde{d}(s)}\right|_{\tilde{v}_{Batt}=\tilde{i}_o=0} = \frac{(1-D)V_{dc} - I_L(Ls+R_1)}{LC_2 s^2 + R_1 C_2 s + (1-D)^2} \\ G_{C,3\_boost}(s) &= \left.\frac{\tilde{i}_o(s)}{\tilde{d}(s)}\right|_{\tilde{v}_{Batt}=\tilde{i}_o=0} = \frac{(1-D)V_{dc}C_2 s + (1-D)^2 I_L}{LC_2 s^2 + R_1 C_2 s + (1-D)^2} - I_L \end{aligned}\right\}, \tag{13}$$

where V_o and V_{in} are the output and input average voltage of the BDC, respectively; L is the inductor of the BDC; C_1 and C_2 are the capacitors of the BDC; V_{Batt} is the battery voltage; R_1 is the internal resistance of the battery. The quantities with tilde, $\tilde{v}_{dc}$, $\tilde{v}_{Batt}$, $\tilde{i}_L$, $\tilde{i}_o$, and $\tilde{d}$ represent the perturbations in various quantities.

3. Proposed Control Strategy For HESS

A control strategy for the HESS based DCMG under islanded mode has been proposed, as shown in Fig. 3. In the developed control strategy, the power generations by both the WT and the PV DGs (P_{G1}) are continuously compared with the total load demand ($P_{L,Tot}$) in the DCMG. When the generated power (P_{G1}) is less than the load demand, this power mismatch is initially fulfilled by the controllable SOFC DG, and then by discharging the BESS. During the surplus power generation, the developed control strategy of the HESS allows to control the charging of the BESS up to its full charging capacity first, and then store the continuously generated surplus power in the H_2SS in islanded mode for all operating conditions. The full charging capacity of the battery means that the battery voltage (V_{Batt}) becomes equal to the maximum voltage of the battery ($V_{Batt,H}$).

In the developed control technique of the HESS, one PI current controller and a pair of PI voltage controllers are suggested for the controlling the operation of the BDC of the BESS. For deficit power case, the power mismatch is initially met by the SOFC DG, and then by discharging the BESS. During discharging of the BESS, the measured DCMG voltage (V_{dc}) has been compared with the reference voltage (V_{dc_ref}), and this error is sent to the PI controller-1, which generates a reference current signal (I_{dch}) for the battery current controller. In case of surplus power generation, the measured voltage of the battery is compared with its high-voltage reference setting ($V_{Batt\_H\_ref}$). This difference of the battery voltage is sent to the PI voltage controller-2 for controlling the charging of the BESS, which provides another reference current signal (I_{ch}) for the battery current controller. This signal will be high (I_{ch}) or zero depending on the charging status of the BESS (V_{Batt_max}). The combination of these two reference current signals (I_{dch} and I_{ch}) provides a reference current signal (I_{Batt_ref}) for the battery current controller and is compared with the measured current of the BESS (I_{Batt}). This current difference is sent to the PI current controller, which generates a controlled reference voltage signal. This controlled reference voltage signal is sent to the PWM generator for providing the controlled duty ratio (D_{BESS}) of the BDC for controlling the operation of the BESS under various operating scenarios.

When the battery has been fully charged, and still the DGs continuously generate the surplus power, the H_2SS is turned on to store this surplus power. For this, the measured DC voltage of the electrolyzer (V_{dc_Elz}) has been compared with the reference voltage ($V_{dc\_Elz\_ref}$), and this error is controlled by the PI controller-3 of the H_2SS.

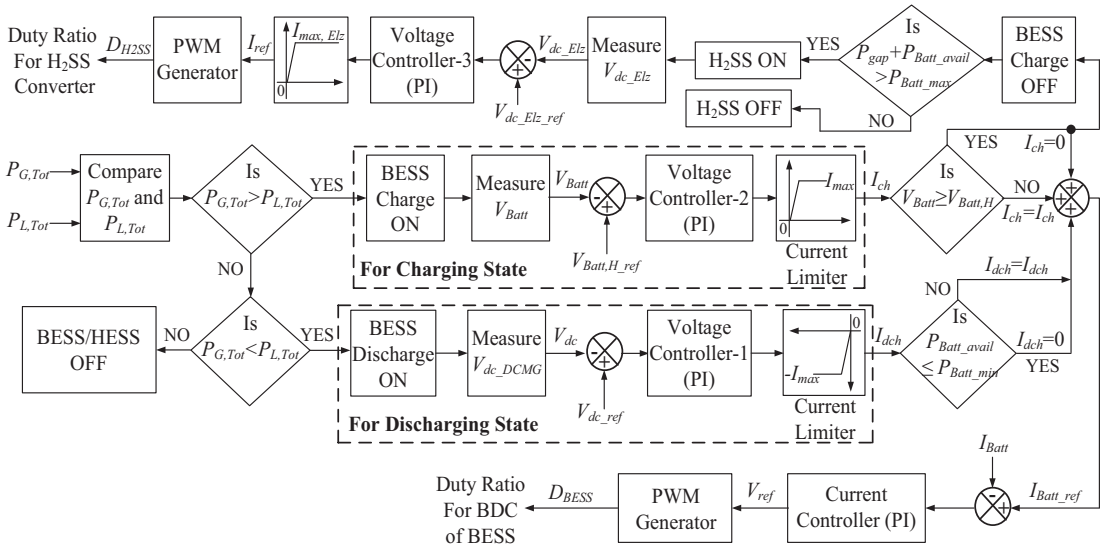

Figure 3. Proposed control strategy of a hybrid energy storage system integrated into the DC microgrid.

Table 1
Values of PI Controllers of DC–DC Converters for the HESS

PI controllers	Proportional gain (K_P)	Integral gain (K_I)
Voltage controllers for BDC	$K_{P\_V} = 246.2 \times 10^{-6}$	$K_{I\_V} = 9.848 \times 10^{-3}\ s^{-1}$
Current controllers for BDC	$K_{P_C} = 353 \times 10^{-6}$	$K_{I_C} = 89.72 \times 10^{-3}\ \mathrm{s}^{-1}$
Voltage controller for buck converter	$K_{P\_V} = 2.5427 \times 10^{-3}$	$K_{I\_V} = 40.68 \times 10^{-3}\ s^{-1}$

The output of this PI controller generates a reference signal, which has been passed through the PWM generator to generate the controlled duty ratio (D_{H2SS}) for the converter of the H_2SS.

The PI controllers' parameters of the DC–DC converters, using the controllable transfer functions given in (9), (12), and (13), have been determined for stable closed-loop system of the HESS, using Bode plot-based technique. The controllers' parameters of the BDC for the BESS with voltage rating 750 V/375 V, and those of the DC–DC buck converter for the H_2SS with voltage rating 750 V/340 V are shown in Table 1.

4. Flowchart for Operation of HESS Based DCMG

A flowchart for the operation of the HESS, connected to the DCMG, is shown in Fig. 4. Initially, the power generations by both WT and PV DGs (P_{G1}), and total load demand of the DCMG are obtained and compared. When the power generated (P_{G1}) is more than the load demand, and the battery is not fully charged, the surplus generated power by WT and PV DGs is used to charge the BESS up to its full charging capacity. When the battery is fully charged, the H_2SS is turned on to store the continuously generated surplus power. When load demand is exactly met by the power generation, the HESS has been turned off. However, during the deficit power case, the load demand is fulfilled by the controllable DG (SOFC), and then by the BESS. If the load is fully met by the BESS, then check for any change in the load and/or the generation. If so, then repeat the process, otherwise, repeat this loop continuously.

When the BESS is also not able to fulfil the load demand, it reduces the load to balance the power in the DCMG, and then check the loop as stated above. The load demand and the power generation in the DCMG are given as follows:

$$\left.\begin{aligned} &P_{G1} = P_{WTG} + P_{PV}, \\ &P_{G,Tot} = P_{WTG} + P_{PV} + P_{SOFC} \\ &\text{and,} \quad P_{L,Tot} = P_{L,3Ph,WTG} \\ &\quad + P_{L,1Ph} + P_{L,DC} + P_{L,Telecom} \end{aligned}\right\}. \tag{14}$$

In the given flowchart and above equation, P_{SOFC}, P_{PV}, and P_{WTG} are power generations by SOFC, PV, and WT DGs, respectively; $P_{L,Tot}$ is the total load demand; $P_{L,1Ph}$, $P_{L,DC}$, $P_{L,3Ph,WTG}$, and $P_{L,Telecom}$ are single-phase AC load, DC load, three-phase load in the WTG area, and telecommunication load, respectively; P_{Batt_avail} is the power available in the battery; P_{Batt_max} is the maximum charging capacity of the BESS; and P_{Batt_min} is the minimum power in the BESS to avoid the battery from the deep discharge.

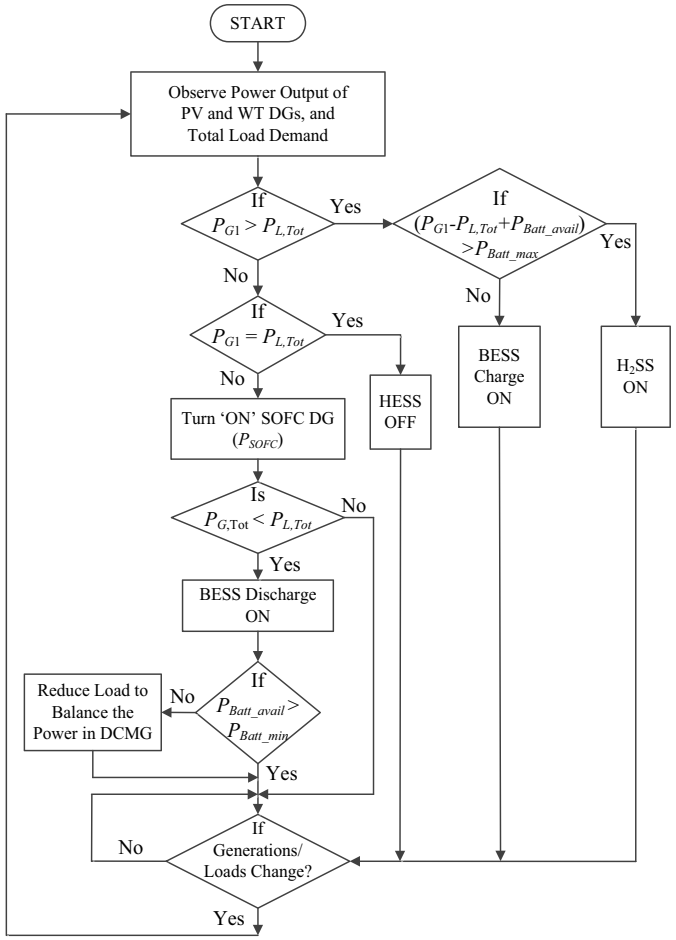

Figure 4. Flowchart for operation of HESS based DCMG.

5. Simulation Results and Discussion

The performance analysis of the developed control technique for the operation of the HESS-based DCMG in islanded mode, as shown in Fig. 1, is carried out for different operating scenarios, for showing its effectiveness.

5.1 Case 1: Variable Loads and Variable Generations

In this mode, the variable total power generation by all DGs, variation of total loads, by assuming constant for

Table 2
Residential Load Variation (Case 1)

Time (h)	00:00	2:00	4:00	6:00	8:00	10:00	12:00	14:00	16:00	18:00	20:00	22:00
Load (p.u.)	0.6	0.51	0.42	0.47	0.64	0.75	0.8	0.85	0.95	1.1	1.0	0.8

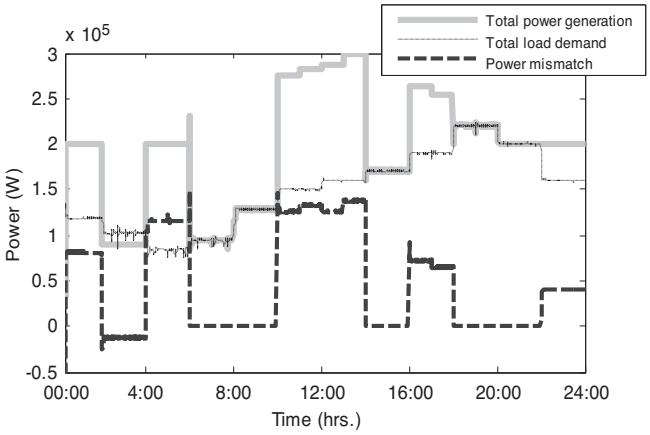

Figure 5. Total load demand, power generation, and power mismatch at DCMG (Case 1).

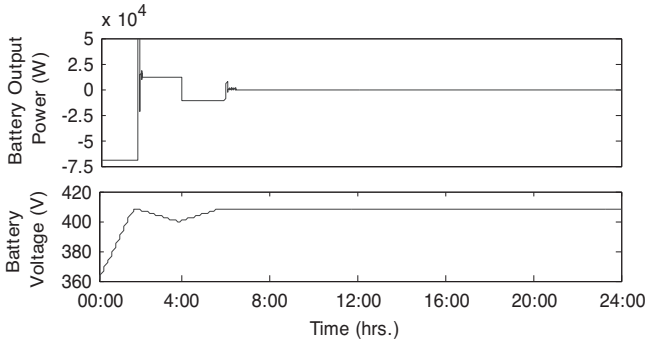

Figure 6. Output power and voltage of battery (Case 1).

the next 2 h as in [19], as shown in Table 2, and power mismatch in the DCMG are shown in Fig. 5. During 00:00–2:00, 4:00–6:00, 10:00–14:00, 16:00–18:00, and 22:00–24:00 h, there is surplus power generation in the DCMG, as shown in Fig. 5. Initially, the BESS has been charged and after being fully charged (*i.e.,* when the voltage of the battery reaches 408.31 V), the remaining generated surplus power is stored continuously in the H_2SS, as shown in Figs. 6 and 7. During 2:00–4:00 h, there is deficit power generation in the DCMG, as shown in Fig. 5, which is met by the controllable SOFC DG up to its peak power capacity and then by the BESS, as shown in Fig. 6. As the BESS becomes fully charged at 6:00 h, as shown in Fig. 6, the continuous surplus power generated is stored in the H_2SS, as shown in Fig. 7. The voltage and current of the electrolyzer of H_2SS, and stored hydrogen, are shown in Fig. 7. Thus, under this mode, the proposed control strategy of the HESS ensures proper power balance in the DCMG under islanded mode.

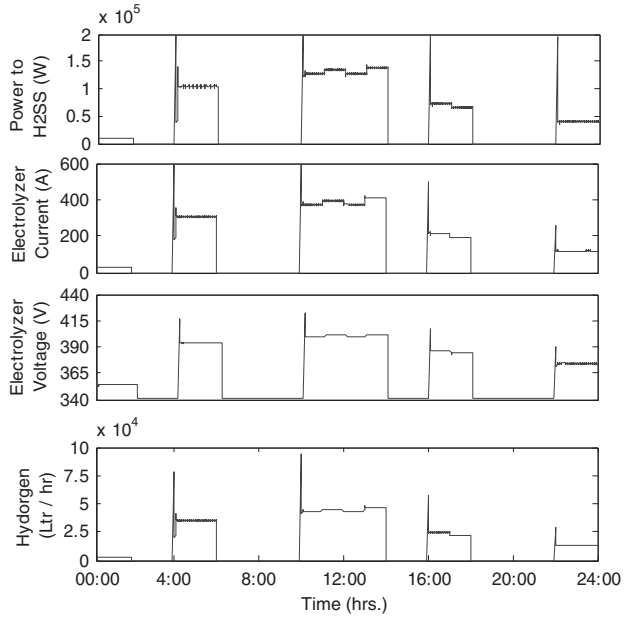

Figure 7. Power to H_2SS, current and voltage of electrolyzer, and stored hydrogen (Case 1).

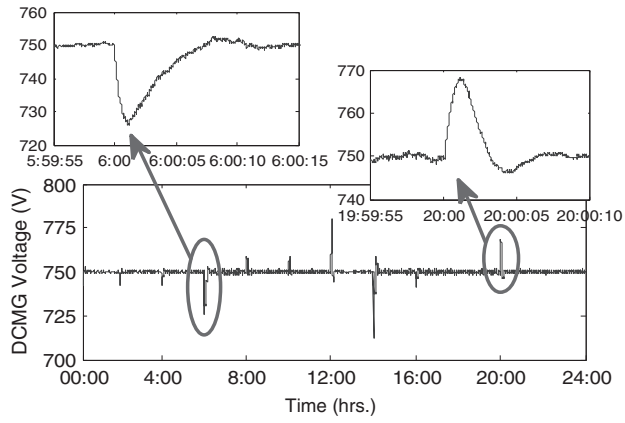

Figure 8. DC voltage of the DCMG (Case 1).

The voltage of DCMG has been established constant, as shown in Fig. 8. The spikes in DC voltage at the time of transients are because of change in the loads and/or generations, as shown in Fig. 8. As we know that as per Indian standards, the permissible voltage regulation in the low-voltage distribution system is ±5% of rated voltage. The rated DC voltage of the DCMG system is considered as 750 V. Therefore, the permissible voltage regulation in the DCMG system is from 705 to 795 V. Thus, the magnitudes of DC voltage spikes in the DCMG, as shown in Fig. 8, are in the allowable regulation range, as given above.

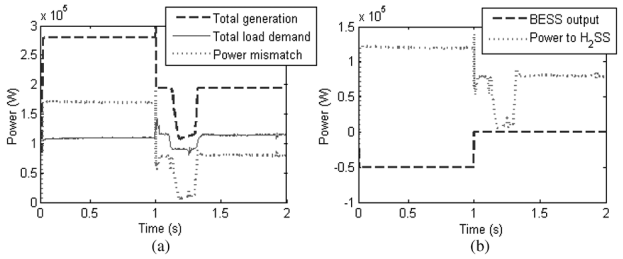

Figure 9. (a) Total load demand, total generation, and power mismatch and (b) BESS output and power to H_2SS during the fault and after the fault (Case 2).

5.2 Case 2: Three-Phase Fault at WT DG Output AC Terminals

In this mode, the output power of the WT DG (at 16.5 and 7.5 m/s wind speed) and PV system are enough to fulfil the load demand. So, SOFC DG is kept in off condition. The total load demand, total power generation, and power mismatch are shown in Fig. 9(a). During $t = 0$ to $t = 1$ s, as shown in Fig. 9(a), there is surplus power generation in the DCMG, which is initially used for charging the BESS, and as at $t = 1$ s, the battery is fully charged. The rest of the surplus power is stored in the H_2SS, as shown in Fig. 9(b). During $t = 1$ s to $t = 2$ s, as shown in Fig. 9(a), there is surplus power generation in the DCMG. As, at $t = 1$ s, the battery is already fully charged, the whole surplus power has been stored in the H_2SS, as shown in Fig. 9(b). The performance analysis of the HESS-based DCMG, under a three-phase symmetrical fault at AC terminals of WTG, has also been carried out in this mode.

At $t = 1.1$ s, a three-phase symmetrical fault, with the fault resistance ($R_f = 10$ mΩ), occurs at AC terminals of WTG. This reduces AC voltage of the WTG from 415 V, line-to-line, rms (1.0 pu) to 62.25 V (0.15 pu), as shown in Figs. 10(b) and 11(b). Under this condition, the output power of the WTG also reduces from 95.9 to 12.5 kW, and the power supplied to the three-phase load of the WTG area also reduces from 25 kW to zero. There is no adverse impact on the power generations by other DGs and on the power supply of the other loads, except for the faulted area load. The total power generation and total load demand are decreased from 194.3 to 110.9 kW and 115 to 90 kW, respectively, as shown in Fig. 9(a). A few part of the surplus power generation (12.5 kW) has been dissipated through the fault resistance, as shown in Fig. 11(a), and the rest of the surplus power is stored in the H_2SS, as shown in Fig. 9(b), even during the fault and after the fault. When the fault has been finished, at $t = 1.3$ s, the DCMG obtains the pre-fault conditions and operates under the normal condition, as shown in Fig. 12. After finishing the fault, the WTG obtains the steady state within the permissible settling time of 40 ms against IEEE-1547 standard, as shown in Fig. 10(b). During the whole operation, the controllable SOFC DG remains turned off.

The voltage of DCMG has been established constant (750 V), under all operating conditions, as shown in Fig. 10(a). At the time of occurrence and clearance of the fault, there are slight transients in the DCMG voltage. These transients settle down within the permissible settling time of 110 ms against IEEE-1547 standard, as shown in Fig. 10(a). The current of the electrolyzer of the H_2SS, voltage of the electrolyzer, and hydrogen production/stored, during the fault, pre-fault, and the post-fault, are shown in Fig. 12.

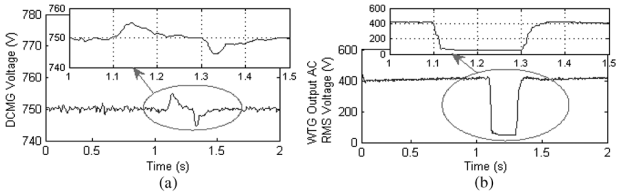

Figure 10. (a) DC voltage of the microgrid and (b) WTG output AC rms voltage during the fault and after the fault (Case 2).

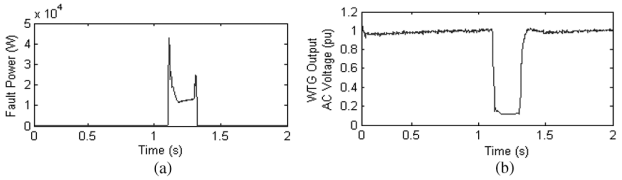

Figure 11. (a) Fault power and (b) WTG output AC voltage during the fault and after the fault (Case 2).

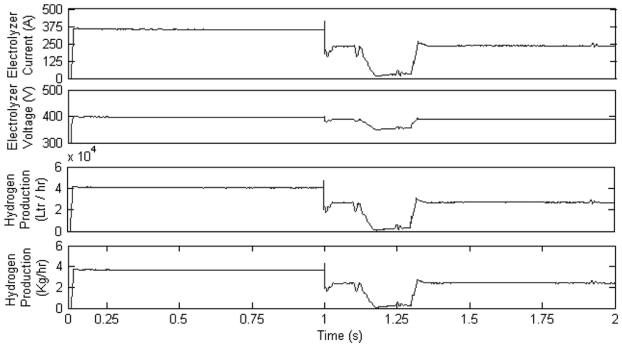

Figure 12. Electrolyzer current, electrolyzer voltage, and hydrogen production during the fault and after the fault (Case 2).

6. Conclusion

In this paper, a control technique of the HESS-based DCMG is developed and tested under islanded mode for all operating conditions. The HESS consists of the BESS and H_2SS, which have been interconnected to the DCMG using the BDC and DC–DC buck converter, respectively. A power control algorithm for power management in the HESS-based DCMG is also proposed. The performance analysis of the HESS-based DCMG along with the developed control schemes has also been presented to show its effectiveness and the robustness for all cases including the fault condition.

The simulation results suggest that the proposed control strategy of the HESS has maintained the power balance at the DCMG in islanded mode, by controlling the operation of the battery up to its full charging capacity, and thereafter to store the continuously generated surplus power in H_2SS for all cases. The proposed control scheme has not allowed any adverse impacts on the loads and/or the generations during fault periods, except slight transients. As the fault is cleared, the DCMG operates under normal mode as in pre-fault conditions. After any disturbance, the system has reached steady state within a permissible settling time of 40 ms – 110 ms against the IEEE-1547 standard. Therefore, the developed HESS-based DCMG along with the developed control technique offers the opportunity of electrification of remote rural areas.

Appendix

The parameters used for the proposed DCMG are shown in Table 3, which have been taken from [1], [3], [7], [9].

Table 3
Main Parameters of the Proposed DCMG

DG	Parameter	Value
WT Generator	*Wind Turbine:*	
	Number of units, N_{wt}	4
	Power of one unit, P_{rated} (kW)	50
	Diameter of rotor,D_b(m)	15
	Swept area, A(m^2)	177
	DFIG:	
	Rated output power, P_{rated}(kVA)	55
	Rated voltage, V_{rated}(V)	415
	Nominal frequency, f_n(Hz)	50
	Number of poles, P	6
	Turns ratio of stator to rotor, n	0.3806
	Resistance/phase of stator, R_s (pu)	0.0071
	Leakage reactance/phase of stator, X_{ls} (pu)	0.171
	Resistance/phase of rotor, R_r (pu)	0.005
	Leakage reactance/phase of rotor, X_{lr} (pu)	0.156
	Mutual reactance, X_m (pu)	2.9
Photovoltaic System	Maximum power, P_{max} (kW)	100
	Number of units in parallel, $N_{p,unit}$	4
	Maximum power of one unit, $P_{max,unit}$ (kW)	25.5
	Maximum voltage, V_{max} (V)	480
	Maximum current, i_{max} (A)	53.2
	Voltage across open circuit, V_{OC} (V)	552
	Current across short circuit, i_{sc}(A)	59.2
	Series modules in one stack, $N_{se,m}$	28
	Stacks connected in parallel, $N_{p,stack}$	13
	Series PV cells in one module, $N_{se,cell}$	36
Solid-Oxide Fuel Cells	Rated power, P_{rated} (kW)	50
	Rated voltage, V_{rated} (V)	340
	Series cells in one stack, $N_{cell,fc}$	380
	Temperature, T (K)	1273
	Ideal potential, E_0 (V)	1.18
	Ratio (Hydrogen to Oxygen), r_{H_O}	1.145
	Ohmic losses, $r\Omega$	0.126
	Peak power capacity, P_{peak} (kW)	90
Electrolyzer for Hydrogen Production	Rated power of a stack of electrolyzer, $P_{Elz,stack,rated}$ (kW)	40
	Series cells in one stack of electrolyzer, $N_{cell,Elz,stack}$	280
	Number of parallel stack in an electrolyzer, $N_{stacks,Elz}$	6
	Reversible voltage V_0 (V)	1.22
	No-load voltage of the electrolyzer, $V_{Elz,0}$ (V)	341.6
	Total rated power of the electrolyzer, $P_{Elz,rated}$ (kW)	240
	Area of one stack of electrolyzer, $A_{Elz,stack}$ (m^2)	0.25
	Overvoltage of the electrolyzer per cell, V_1 (V)	0.185
	Electrolyzer temperature, T_{Elz} (°C)	80
	Number of electrons transferred in each reaction, N_e	2
	Parameter of Ohmic resistance, $r_1(\Omega - m^2)$	8.05×10^{-5}
	Parameter of Ohmic resistance, $r_2(\Omega m^{2\circ}\mathrm{C})$	-2.5×10^{-5}
	Overvoltage coefficient-1, $m_1(A^{-1} - m^2)$	-1.002
	Overvoltage coefficient-2, $m_2(A^{-1}m^{2\circ}\mathrm{C})$	8.424
	Overvoltage coefficient-3, $m_3(A^{-1}m^{2\circ}\mathrm{C}^2)$	247.3

References

[1] M. Kumar, S.C. Srivastava, S.N. Singh, and M. Ramamoorty, Development of a control strategy for interconnection of islanded direct current microgrids, *IET Renewable Power Generation, 9*(3), 2015, 284–296.

[2] B. Wang, M. Sechilariu, and F. Locment, Intelligent DC microgrid with smart grid communications: control strategy consideration and design, *IEEE Transaction on Smart Grid, 3*(4), 2012, 2148–2156.

[3] M. Kumar, S.C. Srivastava, and S.N. Singh, Control strategies of a DC microgrid for grid connected and islanded operations, *IEEE Transaction on Smart Grid, 6*(4), 2015, 1588–1601.

[4] M. Kumar, S.N. Singh, and S.C. Srivastava, Design and control of smart DC microgrid for integration of renewable energy sources, *Proc. IEEE Power & Energy Society General Meeting,* San Diego, CA, USA, 2012, 1–7.

[5] A.A.A. Radwan and Y.A.I. Mohamed, Linear active stabilization of converter-dominated DC microgrids, *IEEE Transaction on Smart Grid, 3*(1), 2012, 203–216.

[6] M. Kumar, Control strategy for back-to-back VSC of DFIG in the wind power generation for smart microgrids, *Proc. of the National Conf. on Advancements & Modern Innovations in Engineering and Technology*, Gurgaon, India, 2020, 1–6.

[7] M. Kumar, S.C. Srivastava, S.N. Singh, and M. Ramamoorty, Development of a new control strategy based on two revolving field theory for single-phase VCVSI integrated to DC microgrid. *International Journal of Electrical Power & Energy Systems, 98,* 2018, 290–306.

[8] S. Teleke, M.E. Baran, A.Q. Huang, S. Bhattacharya, and L. Anderson, Control strategies for battery energy storage for wind farm dispatching, *IEEE Transaction on Energy Conversation, 24*(3), 2009, 725–732.

[9] M.A. Tankari, M.B. Camara, B. Dakyo, and C. Nichita, Ultracapacitors and batteries integration for power fluctuations mitigation in wind-PV-diesel hybrid system, *International Journal of Renewable Energy Research, 1*(2), 2011, 86–95.

[10] P. Karlsson and J. Svensson, DC bus voltage control for a distributed power system, *IEEE Transactions on Power Electronics, 18*(6), 2003, 1405–1412.

[11] F. Lin, Z. Ma, X. You, and T. Zheng, The grid connected converter control of multi-terminal DC system for wind farms, *Proc. of IEEE 18th Inter. Conf. on Electrical Machines and Systems, ICEMS 2005,* vol. 2, Nanjing, 2005, 1021–1023.

[12] N. Gyawali and Y. Ohsawa, Integrating fuel cell/ electrolyzer/ultracapacitor system into a stand-alone microhydro plant, *IEEE Transactions on Energy Conversation, 25*(4), 2010, 1092–1101.

[13] S. Mishra, G. Mallesham, and A.N. Jha, Design of controller and communication for frequency regulation of a smart microgrid, *IET Renewable Power Generation, 6*(4), 2012, 248–258.

[14] http://www.tcisb.com.my/XLPE%20Insulated%20Cables.pdf

[15] R.M. Kamel and B. Kermanshahi, Design and implementation of models for analyzing the dynamic performance of distributed generators in the micro grid part I: micro turbine and solid oxide fuel cell, *Transaction on D: Computer Science & Engineering and Electrical Engineering, 17*(1), 2010, 47–58.

[16] Y. Xia, K.H. Ahmed, and B.W. Williams, Wind turbine power coefficient analysis of a new maximum power point tracking technique, *IEEE Transactions on Industrial Electronics, 60*(3), 2013, 1122–1132.

[17] Y. Mahmoud, W. Xiao, and H.H. Zeineldin, A parameterization approach for enhancing PV model accuracy, *IEEE Transactions on Industrial Electronics, 60*(12), 2013, 5708–5716.

[18] O. Tremblay and L.A. Dessaint, Experimental validation of a battery dynamic model for EV applications. *Journal of World Electric Vehicle, 3*(24), 2009, 1–10.

[19] T.A. Short, *Electric Power Distribution Handbook* (CRC Press, Boca Raton, FL, USA, 2004), 47.

Biographies

Mahesh Kumar (M'11) received his B.Tech degree from IET Lucknow, India, M.Tech degree from National Institute of Technology, Kurukshetra, India, and Ph.D. from Indian Institute of Technology Kanpur, India. Presently, he is an Associate Professor in the Department of Electrical and Electronics Engineering, Amity School of Engineering and Technology, Amity University Haryana, Gurugram, India. His research interests include smart microgrids, integration of renewable energy sources, non-conventional distributed generators, interconnection of clusters of microgrids, PWM-based voltage source converters, and load forecasting. He is a member of the IEEE.

Mylavarapu Ramamoorty (LF) is a Visiting Professor in the Department of Electrical Engineering, Vallurupalli Nageswara Rao Vignana Jyothi Institute of Engineering and Technology, Hyderabad, India. He was a Chancellor at K.L. University, Guntur, India from 2013 to 2019, Common Wealth Fellow at Toronto University Canada from 1965 to1967, and Professor in the Department of Electrical Engineering, IIT Kanpur, India from 1967 to 1977. In 1977, he joined as the Chief of Research at ABB Ltd. Baroda. He joined as the First Director General of CPRI in 1983. He was a Director at Electrical Research and Development Association Vadodara from 1995 to 2007, and then visiting professor at a number of universities abroad. His research interests include applications of power electronics in utilities and industries, power system protection, electrical machines, power quality improvement, faults detection in machines, microgrids, *etc.* He is a Life Fellow of the IEEE, Fellow of INAE (India), and Distinguished Lecturer for IEEE region.